A numerical study on the dissipation mechanisms in sloshing flows induced by violent and high frequency accelerations. Part II: comparison against experimental data.

S. Marrone and A. Colagrossi*

CNR-INM, INstitute of Marine Engineering,

Via di Vallerano 139,

00128 Rome, Italy.

J. Calderon-Sanchez and J. Martinez-Carrascal

School of Naval Engineering,

Universidad Politécnica de Madrid,

Avda. de la Memoria 4 28040 Madrid Spain

(Dated: November 15, 2021)

Abstract

In Paper I of this series [Marrone, Colagrossi, Gonzalez,"A numerical study on the dissipation mechanisms in sloshing flows induced by violent and high frequency accelerations. Part I: Theoretical formulation and numerical investigation"], a theoretical formulation and the numerical model were developed in order to obtain a complete perspective of the energy balance of a violently accelerated flow confined inside a rectangular tank. The tank-fluid system was periodically excited with a predetermined law of motion and the force between the wall and the fluid and the global energy balance were computed. In this second part, the experimental validation of the previous formulation is presented. In order to make a comparison with a previous experimental campaign, where the tank moves along a single degree of freedom mechanical guide, two numerical problems have been studied: in the first, the decaying movement of the tank is prescribed according to the experimental measurements, and in the second the tank is coupled to a mass-spring-damper equation, and the sloshing force produced by the confined fluid acts as an external force. Both problems have been studied for two different fluids, water and oil, which implies a difference of two orders of magnitude in terms of Reynolds number. A complete description of the energy balance inside the fluid tank is performed and the complexity of the fluid dynamic behaviour that takes place inside the tank is explained. The results are compared to the experimental measurements in terms of fluid-wall interaction and energy dissipation.

---

* andrea.colagrossi@cnr.it

I. INTRODUCTION

A theoretical and numerical scheme to compute the dynamics of a confined liquid that moves inside the tank with high accelerations and strong wall impacts, referred to hereinafter as "sloshing flow" or "shaken flow", has been developed in Paper I of the present work.

In this part we will consider the particular fluid-structure interaction problem where the external excitations that generate the fluid movement come from the damped oscillations of a structure. This situation mimics what happens in reality with external wind gusts and air turbulence in fuel sloshing in aircraft wings. In our numerical and experimental model, the fluid is initially confined in a closed tank and accelerated to typical values of 10g in the vertical direction. The initial amplitude is comparable to the tank height and frequencies approximate the Froude scaling law. Previous experiments [15] have demonstrated that the fluid action plays an important damping role on the structure.

First, in order to understand the complexity of the flow involved in the problem and test the fluid Smoothed Particle Hydrodynamics (SPH) solver performance, the system will be uncoupled, and the tank movement will be externally prescribed according to previous experimental records. Second, the fully coupled system is solved where a sloshing forced mass-spring-damper system is coupled with an SPH code that computes the fluid action. The results obtained in this coupled case are compared to their previous equivalent experiments [15]. Similarly to the procedure followed in [5, 6] the extra damping added by the fluid's presence is computed numerically and compared to the experimental results.

Following the terminology explained in the introduction of Paper I, in decaying excitation flows an impulsive heave motion of the tank produces a violent slamming against the top and bottom tank walls. This initial stage of these violent flows, referred to as "shaken flow", is essentially driven by inertial forces which are much larger than the gravitational ones.

These kinds of sloshing flows can be studied either experimentally or computationally using different techniques. Regarding the experimental studies the first references can be found during the mid-1960s [1, 8, 10]. These experiments normally study horizontally moving tanks, or rotating tanks but only a few recently published studies focus on violent vertical tank movements [7, 14]). In a recent experimental campaign [18] a partially filled tank was attached to the end of an elastic beam trying to reproduce the scaled situation found in aircraft wing tanks. The beam was deformed and released, and the tank containing the fluid

3

would move with a decaying, heave, oscillatory motion characterized by a peak acceleration near 10g. This behaviour has been also reproduced in the experimental campaign developed in the CEHINAV [15] and in the University of Bristol [11] based on a series of single degree of freedom vertical sloshing experiments. In this work, a Froude scaled experiment has been devised measuring the sloshing force acting on the tank when the accelerations are similar to the ones found in a real wing, confirming that the fluid presence notably increases the damping of the system. Ongoing projects, such as the EU-SLOWD [13] are planning ambitious experimental campaigns in the future that include a full scale aircraft wing structure with corresponding fuel tanks. This structure will be excited to the most critical conditions where sloshing effects are likely to be relevant.

Regarding the numerical approach, in agreement with the first part of this work, a SPH method has been used. The important improvements of the classical SPH method explained in Part I are now applied to different decaying cases. As was discussed, these new ideas are very important when violent free surface flows with strong wall impacts are computed using the SPH methodology, showing its reliability in problems involving free-surface breakage, which occurs frequently during violent sloshing. Alternatively, different techniques can be used in order to solve the fully coupled problem involving fluid and structural motions. For example, in [12] the potential flow theory is used, whilst [19] and [17] use a a mass-spring system.

As in the first part of this work, this paper is not limited to obtaining accurate simulations of these violent sloshing flows; it also tries to study the energy dissipation mechanisms that occur in these kinds of violent and confined flows which, eventually, are of interest in aeronautics applications.

This work is organized as follows: Section 2 describes the experimental setup used for the validation of the numerical results. Section 3 briefly recalls the adopted mathematical model which is described in detail in the first part of the paper (Part I). The results of the numerical simulations for both forced motion and fully coupled tests are presented in Section 4. Finally, the main findings are summarized in the conclusions section.

II. EXPERIMENTAL MODEL FOR THE VALIDATION

In [15], the experiment by [18] was simplified into a Single Degree of Freedom (SDOF) vertically moving tank and represents a more damped version of the experiment conducted by [11] in 2021. Taking into account the dimensional analysis of the problem at hand and applying the Π theorem to a reference variable [3], for example the damping ratio added by the fluid to the system, one can find a dimensional relation between this variable and several non-dimensional groups, such as the Reynolds number, Froude number, density ratio, etc. In sloshing problems, a Froude scaling is usually performed [3] where $Fr = \sqrt{\omega_0^2 H / Ng}$ is defined based on the maximum acceleration of the problem which is N times the gravity. In the Froude number definition, ω_0 represents the characteristic angular frequency of the problem, H represents the height of the tank, Ng is the maximum acceleration of the problem, being $N \approx 10$ in this study. Next, a geometrical scaling parameter is considered $\lambda = H_{SDOF}/H_W$ defined as the ratio between the heights of the SDOF tank and the wing tank. For the SDOF sloshing tests, a 1:5 scale was selected ($\lambda = 0.2$) which results in a tank geometry of 10×6×6 cm. The scaled tank is filled up to 50 % of its volume which results in a water mass of $m_l = 0.18$ kg and it oscillates at a characteristic frequency of $f_0 = 6.51$ Hz.

A photograph of the experimental setup at the Model Basin Research group sloshing laboratory of the UPM and a simplified outline are shown in figure 1. The experimental rig is an SDOF system composed of a mechanical guide that allows the single degree of freedom constraint. This guide is attached to a C-shaped wooden structure that holds the tank with a structural mass of $m_s = 2.403$ kg. Similarly, the C-shaped wooden structure is attached to a set of 6 springs, each one having an individual spring constant of $k = 718.05$ N/m, 3 on the upper side and 3 on the bottom side. The lower springs are mechanically embedded into the floor, and on the opposite side the upper set of springs is attached to a metallic plate that acts as a joint between them and the embedded load cell. This setup also includes an accelerometer attached to the C-shaped wooden structure, a laser sensor aimed at the wooden block and two solenoids acting as a release mechanism. The structure is deflected to an initial amplitude and it is fixed by the magnetic force of the solenoids. When the electrical current is turned on, the structure is released triggering the beginning of the experiment. The acceleration and position of the tank as well as load cell measurements are recorded allowing the calculation of the sloshing force acting on the system. A more

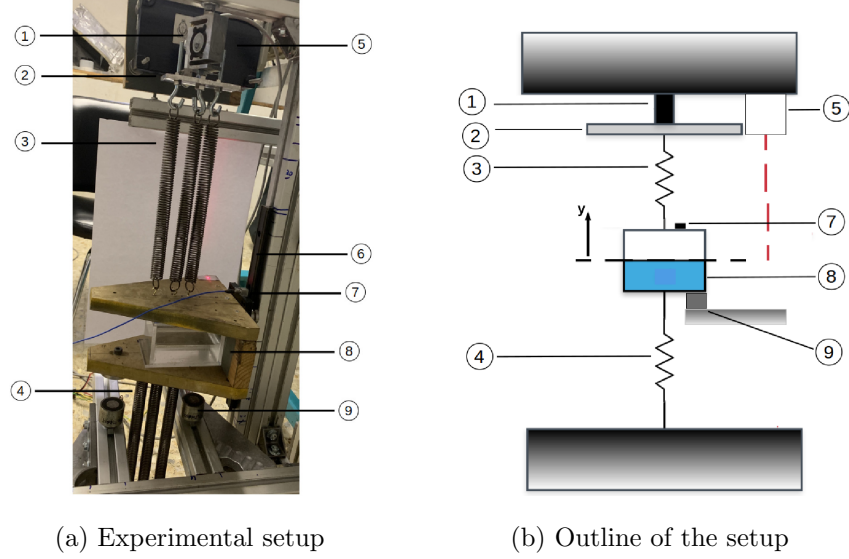(a) Experimental setup　　　　　(b) Outline of the setup

FIG. 1: Experimental setup and outline. (1) Load cell, (2) Metallic plate with mass $m_p = 0.06$ kg, (3) Upper set of springs with stiffness constant $k_1 = 2154.17$ N/m, (4) Lower set of springs with stiffness constant $k_2 = 2154.17$ N/m, (5) Laser sensor, (6) Mechanical guide, (7) Accelerometer, (8) Methacrylate tank and C-shaped wooden structure with mass $m_s = 2.403$ kg, (9) Pair of solenoids acting as release mechanism.

t = 0.108 s　　　　t = 0.130 s　　　　t = 1.27 s　　　　t = 2.45 s

FIG. 2: Experimental snapshots of the SDOF vertical sloshing water experiments carried out in [15] for 10 g and 50 % filling level.

detailed description of the experimental setup and vertical sloshing force derivation can be found in [15].

In figure 2 it can be seen that the flow is divided into four main stages. First, right after the release at $t = 0.108$ s the meniscus present in the hydrostatic state travels horizontally forming a ripple at the free surface that triggers a vertical Rayleigh-Taylor instability. The instability travels in the upward direction and causes the first fluid to wall impact

6

at $t = 0.130$ s. After that, the free surface is fragmented and the flow can be considered as highly turbulent, characterized by many fluid-fluid and fluid-wall impacts. Finally, when the tank motion is attenuated, at around $t = 2.45$ s the last fluid-wall impact happens and a standing wave regime develops until the system reaches the rest condition.

From this experimental study, the vertical sloshing force, tank acceleration and position are obtained. Each experimental test was repeated three times, finding very small variability among repetitions. These results are used in Section IV to validate the numerical outcomes.

III. BRIEF RECALL OF THE ADOPTED MODEL

In this section, the main hypotheses underlying the numerical model and the equations of the system's energy balance are briefly recalled. For a complete derivation and discussion of the hypotheses and the equations described below, the reader is referred to the first part of the paper (Part I).

The governing equations adopted are the Navier-Stokes equations (NSE) for a single-phase weakly-compressible fluid. Because of the high Reynolds number related to the experiments described in the previous section, in the numerical scheme a sub-grid model for the turbulent viscosity is needed. To this end the δ-LES-SPH model described [2] is considered, where a Large Eddy Simulation (LES) modeling is rewritten in a Lagrangian formalism and introduced in the SPH system of equations.

The main simplifications adopted in the numerical model to reproduce the experiment are:

- a two-dimensional framework;

- the air phase is neglected (only the liquid phase is modelled);

- thermal conductivity and surface tension effects are neglected;

- weakly-compressible regime is always attained using a sufficiently large artificial speed of sound .

Furthermore, in simulations involving water, the adopted spatial resolution is not sufficient to resolve the Wall Boundary Layer (WBL) regions and, for this reason, the free-slip conditions are used. Conversely, for simulations involving oil, due to the lower Reynolds

7

number it is possible to resolve the WBL regions, and therefore, for these simulations the no-slip conditions are used. In Appendix A a study of the relevance of WBL modelling is addressed.

Due to its easier implementation in Part I of the paper the implementation of the Non-inertial Frame of Reference (Ni-FoR) is preferred with respect to the Inertial Frame of Reference (I-FoR). This is also because it avoids numerical errors related to the tank motion. This choice is made in the present work as well. Besides the technical numerical aspects, the energy balance written in both of the frames of reference will be useful for the analysis of the data and the comparison against the experimental measurements.

Recalling the derivation in Part I, the δ-LES-SPH energy balance can be written as:

$$\dot{\mathcal{E}}_M + \dot{\mathcal{E}}_C = \mathcal{P}_V + \mathcal{P}_V^{turb} + \mathcal{P}_\mathcal{N} + \mathcal{P}_{ext}, \qquad \mathcal{P}_\mathcal{N} := \mathcal{P}_\delta + \mathcal{P}(\delta\boldsymbol{u}) \tag{1}$$

where $\dot{\mathcal{E}}_M$ is the time derivative of the mechanical energy of the particle system, $\dot{\mathcal{E}}_C$ is the time derivative of the elastic potential energy associated to fluid compressibility, $\mathcal{P}_{ext}$ is the external power due to the tank motion. The terms $\mathcal{P}_V$, $\mathcal{P}_V^{turb}$, and $\mathcal{P}_\mathcal{N}$, are power terms related only to energy dissipation: $\mathcal{P}_V$ and $\mathcal{P}_V^{turb}$ correspond respectively to fluid viscous stresses and modelled turbulent viscous stresses, and $\mathcal{P}_\mathcal{N}$ is related to numerical diffusive terms. The energy dissipated in the numerical scheme, $\mathcal{E}_{diss}$, is therefore directly evaluated as:

$$\mathcal{E}_{diss} = \int_{t_0}^t \left(\mathcal{P}_V + \mathcal{P}_V^{turb} + \mathcal{P}_\mathcal{N} \right) dt . \tag{2}$$

IV.   RESULTS: SLOSHING IN FORCED DECAY HEAVE MOTION

In this section the experiment described in Section II is addressed. The problem is studied following two steps of increasing complexity.

- Test N.1: the acceleration time history recorded in the experiments in [15] is applied to the tank. In this case it is possible to also compare the forces obtained in the numerical simulation with those recorded in the experiment.

- Test N.2: the complete coupled Fluid Structure Interaction (FSI) problem is considered. In this case one can directly compare the observed numerical tank displacements to the experimental ones, also avoiding the uncertainties related to the computation of the experimental work done by the tank.
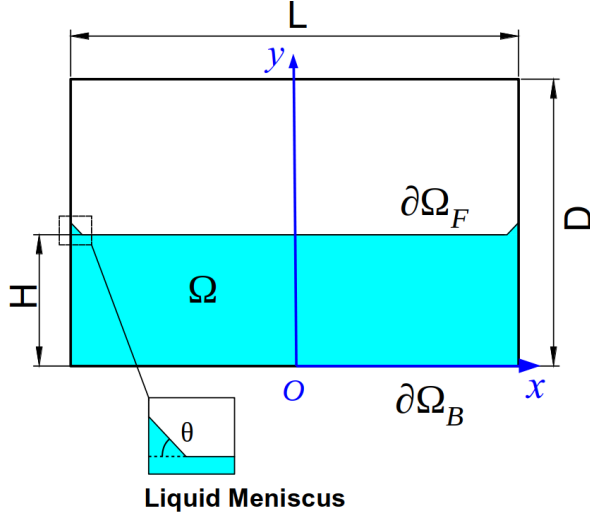
8

FIG. 3: Sketch of the problem geometry and initial conditions (see Part I for more details).

For all the test cases the numerical setup is the same as the one described in Part I. Specifically, the tank height is D=0.06 m, the width is L=0.1 m and the tank filling level is 50%, that is, the water depth is H=0.03 m. The liquid used is characterised by density $\rho = 1000$ kg/m^3 and corresponding viscosity in order to match the desired Re for each fluid.

In the experiment, when the fluid is at rest, a meniscus is formed close to the vertical walls because of the surface tension. This is numerically replicated in the initial conditions by adding, close to the vertical boundaries, a small fluid triangle of the same angle and height as in the experiment (figure 3), respectively $\theta = 45°$ and $l = 1.5$ mm. As it is also reported in Part I, surface tension effects are negligible in terms of damping added to the system. This has already been studied by [9]. The speed of sound adopted in all the simulations of the present section is the same as in Part I, $c_0 = 40$ m/s.

A. Test N. 1: Sloshing in forced motion: experimental damped motion law

In this section the law of motion resulting from the experiment in [15] is imposed on the tank. Distinct from the test case in the first part of the paper (Part I), here the law of motion presents an exponential decay due to the energy that is quickly dissipated by the liquid, and to a lesser extent, by the springs and the supporting rails. In addition to the study of the energy dissipation under decaying motion, this test case allows for a comparison of the obtained forces (and related work) acting on the tank with those recorded in the experiment.
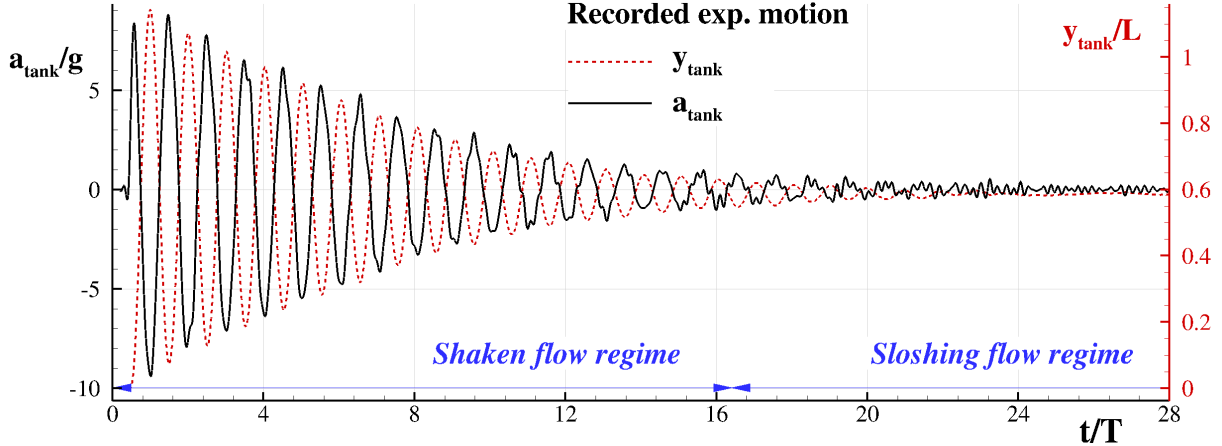
9

FIG. 4: Tank motion recorded in the experiment of [15] plotted in terms of elevation (dashed line) and acceleration of the tank (solid line).

The maximum amplitude of the oscillation motion, taken from recordings in the experiment, is $2A/L = 1.14$. The frequency of motion is defined as $f_0 = \sqrt{k/m}/(2\pi) = 6.51$ Hz where k is the total spring stiffness and m the sum of the masses of the tank, the liquid and the springs. The period $T = 1/f_0 = 0.154$ s will be used as a characteristic time scale. We can define the characteristic velocity to be $U_{max} = 2\pi A/T = 2.33$ m/s. The corresponding Reynolds number depends on the fluid tested. The reference case used in this work corresponds to water, with Re$= \rho U L/\mu = 233,000$, with dynamic viscosity $\mu = 0.001$ Pa $\cdot$ s. Throughout the session the dissipated energy, $\mathcal{E}_{diss}$, is made non-dimensional by the potential energy $\Delta\mathcal{E} = \rho L H g 2A = 3.355$ J, unless otherwise specified, corresponding to a power in one cycle equal to $\Delta\mathcal{P} = \Delta\mathcal{E}/T = 21.84$ W. In figure 4 the recorded motion of the tank is plotted in terms of elevation and acceleration of the tank. In the same figure the portion of the time evolution for which the flow is in the "shaken flow" regime is highlighted. We define here the "sloshing" regime as starting when $a_{tank}/g \leq 1$, a_{tank} being the tank acceleration.

In figure 5 the energy decay obtained by the SPH simulation is reported along with the tank displacement. In this case the adopted resolution is $N = H/\Delta x = 400$. The same stepped shape of the simulations in Part I can be recognised in the first 5 periods of oscillation. However, in the present case the rate of dissipated energy decreases in time and becomes very small when the flow is in the sloshing regime. In the same figure, the analytical solution by the 1D model described in Part I (Section VII C) is also reported. It represents a

lower boundary of the system energy and in this case where only the δ-LES-SPH results are discussed, it is far too dissipative with respect to the numerical simulation. Note that, when the "shaken" flow regime ends, the 1D model does not predict any dissipated energy any more. This is due to the hypotheses underlying this simplified model: energy is dissipated only through impacts against either the ceiling or the bottom of the tank.

In the same figure 5, some relevant instants of the flow are labelled. Labels a) to d) are reported in figure 6, in terms of free-surface configuration and contour of the turbulent viscosity ratio μ_T/μ. The initial flow evolution is analogous to the periodic case but for the time of the first impact: in the present case the impact occurs at t/T=1.26 whereas in the previous case it happened at t/T=0.64. This is due to the lower acceleration acting in this case which causes a delayed detachment of the flow. Apart from that, the flow evolves in the same way: in a) the Rayleigh-Taylor instability is triggered; in b) the fluid impacts against the tank ceiling with production of small jets on the sides and high velocity gradients in the center where the two main jets collide; then, the fluid starts a series of cyclical impacts against the bottom of the tank as in c) and d), in which two impacts at the tank bottom are shown: the fluid is mostly fragmented in multiple jets and the energy is mainly dissipated in free-surface re-connections and the consequent generation of vorticity.

The values observed for the ratio μ_T/μ in plots b), c) and d) are order $\mathcal{O}(1)$. Following the analysis presented in Part I, this represents an indication that the inertial turbulent scale is resolved. However, as shown below in the analysis of the energy components, a further increase of the resolution would be needed even if at $N = 400$ the result is close to its convergent limit.

In figure 7, the flow evolution at the time instants related to labels e) and f) of figure 5 is shown in terms of vorticity contours. These two time instants are representative of the transition from the "shaken" flow regime to the "sloshing flow" regime: in plot e) the flow is still highly fragmented with production of vorticity distributed on a wide range of length scales; in f) the vorticity intensity is strongly reduced and no roof impacts occur anymore: the fluid appears compact with very small local breakings and a large gravity wave travels on the liquid surface. This is the typical behaviour of moderate sloshing flows.

In the left plot of figure 8 the different energy components are reported. The amount of energy dissipated through resolved viscous stresses is 8.6%, which is similar to the result obtained for the periodic case presented in Part I. At the same time, the term related
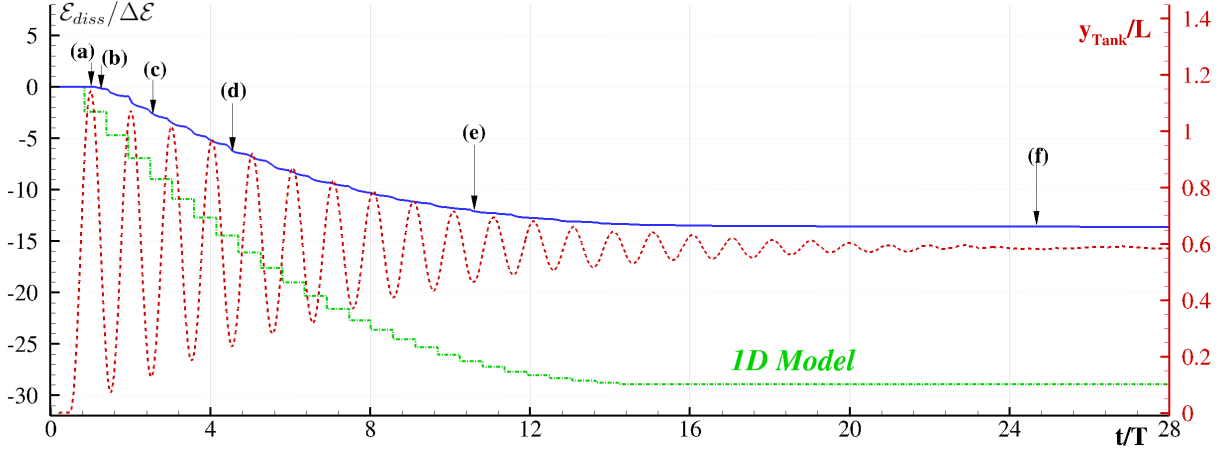
FIG. 5: Time history of the energy decay obtained by the SPH simulation at $N = 400$ and by the 1D analytical model as described in Part I (solid lines). The dashed line represents the tank elevation. Labels (a) to (f) correspond to the same time instants of figure 6 and 7.
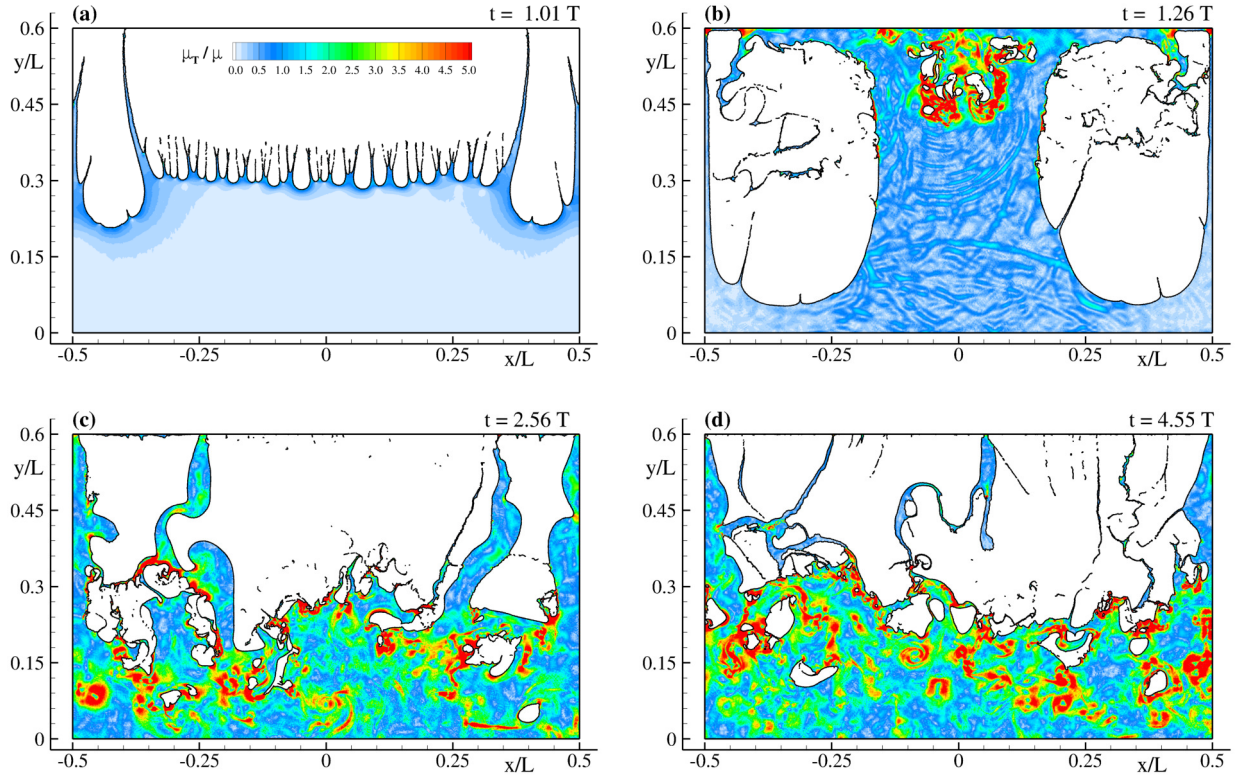

FIG. 6: Four representative instants of the flow evolution obtained by the SPH simulation at $N = 400$ for the Re=233,000 case. Contours refer to turbulent viscosity ratio μ_T/μ.
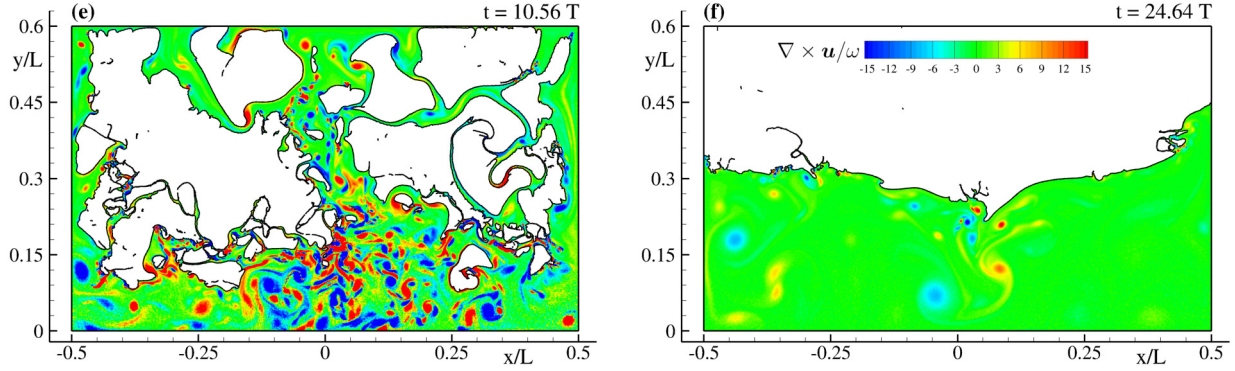
FIG. 7: SPH simulation at $N = 400$ for the Re=233,000 case: vorticity contour at $t/T = 10.56$ (left plot) and $t/T = 24.64$ (right plot).

to numerical energy dissipation, $\mathcal{E}_{\mathcal{N}}$, is decreased to 24.2% of the total dissipated energy. As already mentioned in Part I, $\mathcal{E}_{\mathcal{N}}$ is mainly related to energy diffusion in impacts, and therefore, in this problem and for the resolutions adopted it plays a non-negligible role. In order to investigate the numerical convergence for this problem, the same procedure described in section VII F of Part I has been applied: four spatial resolutions have been considered, namely $N = H/\Delta x$=50,100,200 and 400; and for each discretization 10 repetitions of the same simulation have been performed applying a noise of $0.01\Delta r$ on the initial lattice. The result of this study is summarized in the right plot of the figure 8. Each curve represents the ensemble average of the 10 repetitions of the same simulation and the error bars indicate the standard deviation.

Conversely to the periodic test case, the numerical solution exhibits a more marked convergence in terms of average curves. The convergence is on the order of about 1.5. Note that in the periodic case the Re is about twice the present case and that decay motion implies a decreasing turbulent motion in time. Regarding the standard deviation, this does not monotonically decrease with the increasing resolution. A possible reason is related to the limited time history of the simulation. In fact, in the short time range the variability becomes prominent, the flow not being driven by a long-term periodic forcing.

In order to better investigate the role of viscous effects, the same simulation has been conducted by drastically reducing the simulation Reynolds number. To this end, the considered liquid has been changed to oil, which has kinematic viscosity of $5 \cdot 10^{-5}$ m^2/s corresponding to Re=4,660 (oil density $\rho = 900$ kg/m^3, dynamic viscosity $\mu = 4.5 \cdot 10^{-2}$
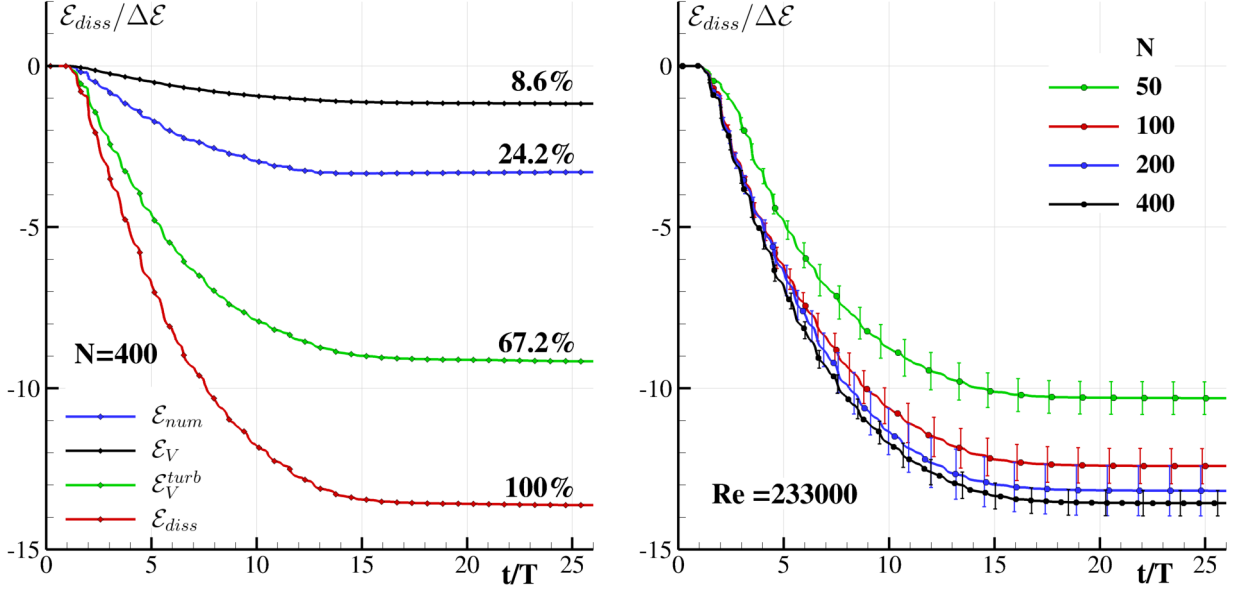
FIG. 8: Left: time history of the energy components defined in Section III: resolved
viscous dissipation $\mathcal{E}_V$, modelled turbulent viscous dissipation $\mathcal{E}_V^{turb}$, numerical diffusion
$\mathcal{E}_\mathcal{N}$, total energy dissipation $\mathcal{E}_{diss}$ for the case $N = 400$ and Re=233,000. Right: ensemble
average of of the energy dissipation $\mathcal{E}_{diss}$ time history for resolutions $N = 50$, $N = 100$,
$N = 200$ and $N = 400$; error bars refer to the computed standard deviation.

Pa· s). In this case the energy terms are made non-dimensional through the potential
energy $\Delta\mathcal{E} = \rho\,LHg2A = 3.020$ J. The spatial resolution is again $N = 400$. As mentioned
in Section III, for this simulation no-slip wall boundary conditions are used due to the
relevance of boundary layers for this test case. Indeed, using the Blasius theory as in Part I,
the thickness δ_{BL} of the wall boundary layer for this case is estimated to be $H/\delta_{BL} = \mathcal{O}(10^2)$
which can be adequately resolved with the adopted spatial discretization.

In figure 9 the flow evolution for the same time instants as in figure 5 is reported. Due
to the greater viscosity, the liquid does not truly impact against the roof in the first cycle
of the tank motion: only two thin jets go to the ceiling at $t = 1.18T$, but the bulk of the
flow has not got enough kinetic energy to reach it when the tank acceleration inverts its
motion (top-right plot of figure 9). Notwithstanding, the small jets are energetic enough to
disrupt the compact shape of the fluid when they fall back down, generating large vortical
structures. In the bottom plots of figure 9 the contour plots of the ratio μ_T/μ are shown for
two bottom impacts corresponding to labels c) and d) of figure 5. In this case the highest

14
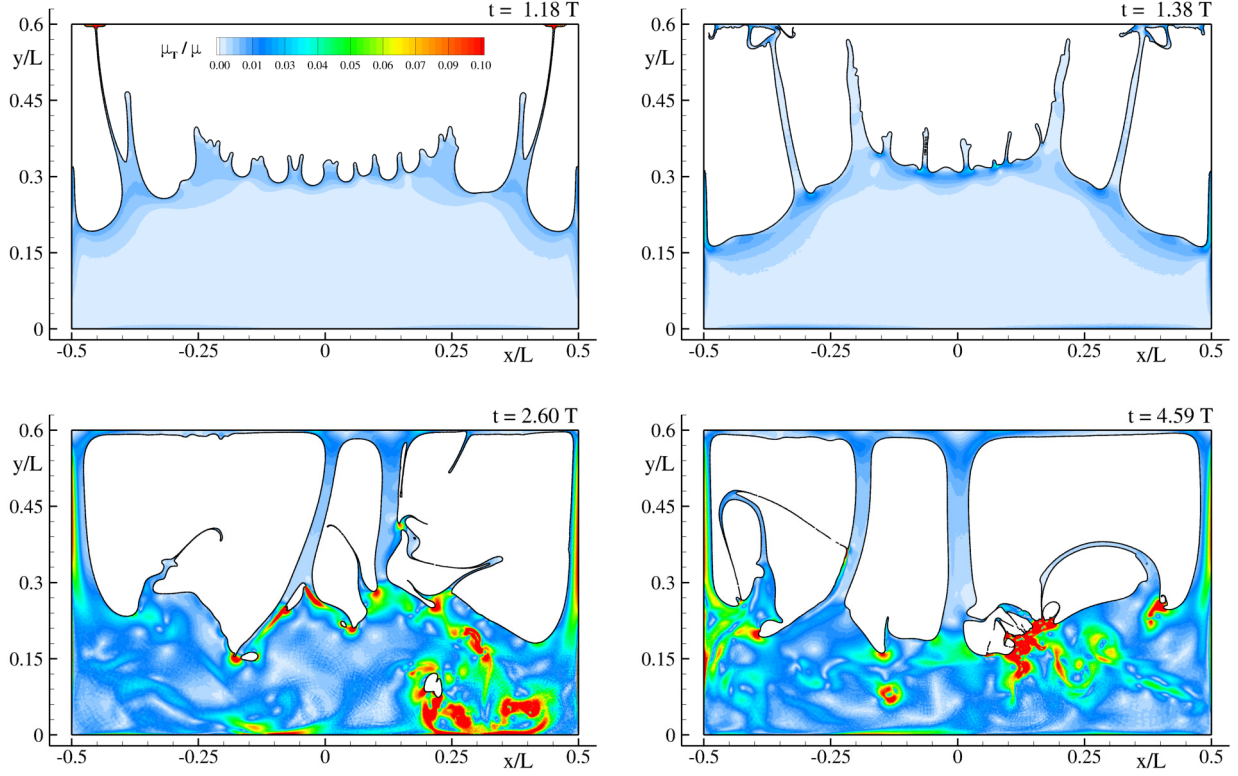
FIG. 9: Four representative instants of the flow evolution obtained by the SPH simulation at $N = 400$ for the Re=4,660 case. Contours refer to turbulent viscosity ratio μ_T/μ.

values attain $\mu_T/\mu = 0.1$, showing that the solution is now close to a DNS.

At this viscosity level, the main eddies are much larger with respect to the water case, as shown in figure 10: vortical structures are few and cover a narrow range of length scales. Also, the vorticity generated at the boundaries represents a large portion of the total vorticity. The wall boundary layer is discretized with about 10 particles for this spatial resolution, confirming the appropriateness of the above estimation. In the right plot of figure 10 the vorticity field is reported for the same instant as label f) of figure 7. Most of the flow's mechanical energy has been dissipated, and as a consequence the free surface is smooth and no vortices are generated anymore.

In the left plot of figure 11 the dissipative energy components are reported. The most prominent energy component in this case is represented by the resolved viscous term $\mathcal{P}_\mathcal{V}$, which at the end of the simulation amounts to 74% of the total dissipation. The numerical dissipation $\mathcal{E}_\mathcal{N}$ is almost halved with respect to the case with water whereas the modelled turbulent viscous energy dissipation is dramatically reduced. This reflects the fact that at
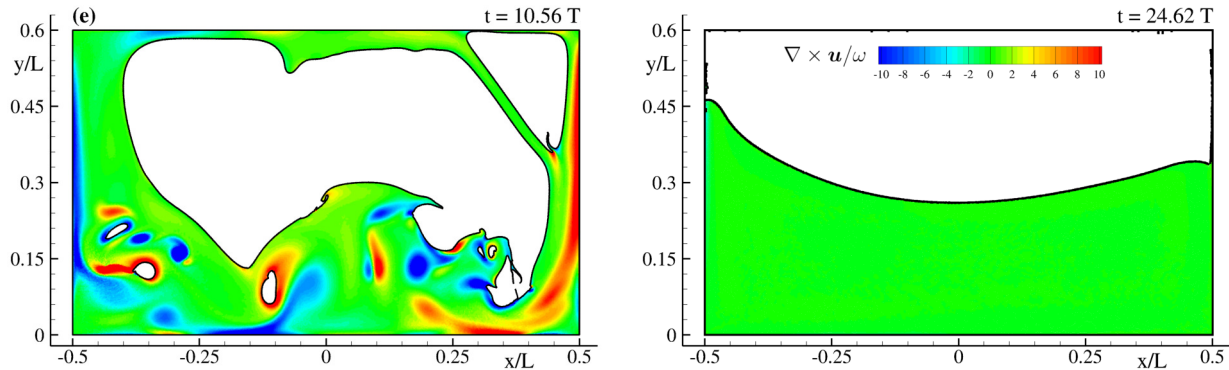
15

FIG. 10: SPH simulation at $N = 400$ for the Re=4,660 case: vorticity contour at the same time instants of figure 7.

this Re a large portion of the viscous dissipation is resolved and the remaining amount of residual energy is dissipated during impacts by means of the power terms $\mathcal{P}_N$ and $\mathcal{P}_V^{turb}$.

Also for this test case the convergence study (right plot of figure 11) has been performed in terms of ensemble average of the energy time history. Differently from the water test case, only three spatial resolutions have been considered, namely $N = 50, 100$ and 200; and 10 repetitions of the simulations have been performed. In this case it is clear that the average solution does not depend significantly on the spatial resolution. This fact suggests that the adopted LES filter lies well below the inertial range for all the adopted discretizations [16], and therefore, even for the coarsest resolution the obtained solution is an acceptable representation of the large eddies developed in the flow. Further, the standard deviation is largely reduced, which is an expected behaviour for this lower regime of Reynolds number, contributing to decreasing the uncertainty of the obtained solution.

It is worth noting that in the oil test case the total amount of non-dimensional dissipated energy is lower with respect to the water one. This result is, indeed, consistent with the findings in [4] where similar results were found experimentally. In particular, it was explained that water sloshing flows dissipate energy mostly through energetic impacts and breaking wave phenomena. Therefore, in liquids characterised by higher viscosity as in the oil case, the breaking events are less intense, and therefore less dissipative. On the top of that, oil is 0.9 times less dense than water, which further enlarges the dimensional energy dissipation difference between both fluids. Clearly, for these kinds of problems, in [9] it is emphasized that density variations have substantial effects on energy dissipation with respect to viscosity,
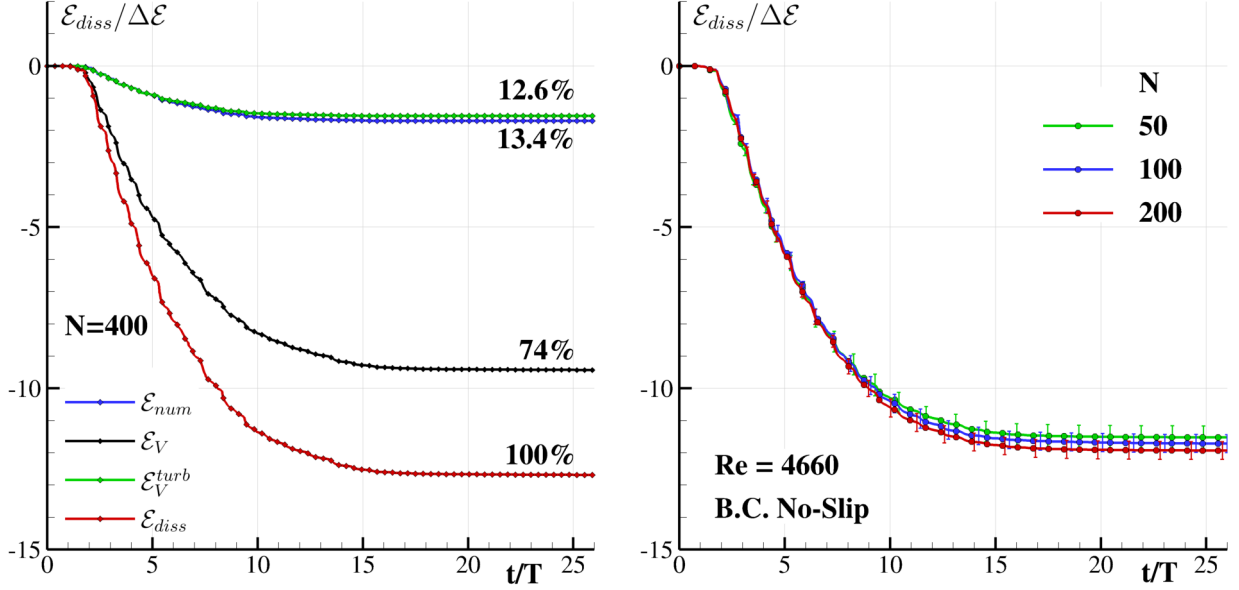
FIG. 11: Left: time history of the energy components defined in section III: resolved viscous dissipation $\mathcal{E}_V$, modelled turbulent viscous dissipation $\mathcal{E}_V^{turb}$, numerical diffusion $\mathcal{E}_\mathcal{N}$, total energy dissipation $\mathcal{E}_{diss}$ for the case $N = 400$ and Re=4,660. Right: ensemble average of of the energy dissipation $\mathcal{E}_{diss}$ time history for resolutions $N = 50$, $N = 100$, $N = 200$; error bars refer to the computed standard deviation.

especially when Re $> 10^4$.

As far as the CPU costs are concerned, ten cluster nodes equipped with dual 12-core Intel Xeon (Haswell) E5-2680v3 processors at 2.5 GHz, were used for 15 days to perform the 90 simulations. The only ten simulations with N=400, performed for the water case, required 8.4 days using the ten cluster nodes (*i.e.* 240 cores). The above CPU costs are practically the same of those requested to perform the simulations discussed in the Part I. The whole 122 simulations executed for the present research investigation (Part I and Part II) required an overall amount of one month of calculation on 10 cluster nodes.

Validation against the experimental vertical forces

The vertical forces obtained in the numerical simulations are here compared to those measured in the experiment for the water case, as a validation of the numerical outcome. In figure 12 the vertical forces obtained for resolutions $N = 50, 100$ and 200 are reported

17

in terms of average ensemble over the 10 repetitions performed for each spatial resolution. Remarkably, only small discrepancies are observed between the different resolutions. This is to be ascribed to the inertial forces which account for a large part of the total force. To better appreciate this, in the same figure the non-dimensional F_y^{stat} component (see Part I for a definition) is reported. At the beginning of the simulation, when the Rayleigh-Taylor instability has not developed yet, the computed forces are trivially equal to the inertial ones. After t/T=1 the flow detaches from the bottom and the hydrodynamic forces come into play. However, their role remains limited with respect to inertia, apart from the first oscillations where the violent impacts cause a sharp peak of the vertical force.

In figure 13 the computed force at $N = 400$ is compared to the experimental observation. Note that experimental data are filtered through a $4th$ order Butterworth filter with a cutoff frequency of $f_{cut} = 7.7 f_0 = 50$ Hz (see [15]) In the top plot of figure 13 the numerical vertical force F_y is compared to the experimental measurement. The numerical outcome is, generally, in good agreement with the experiment, especially if one considers the different approximations inherent in the adopted numerical model. In the initial stage of the simulation, around $t/T = 1$, a large discrepancy is observed. At this stage, in the numerical simulation the flow has not impacted yet against the roof (see figure label (a) of 6). Therefore, this could be due to a non-perfect action of the release mechanism in the experiment, or to differences in the initial flow deformation.

In bottom plot of figure 13 only the hydrodynamic component of the vertical force is compared, namely F_y^{dyn} (see Part I equation 21 for a definition). This comparison is more challenging than the previous one, as a large part of the total force is represented by F_y^{stat}. In this sense, it is also more appropriate to compare only the F_y^{dyn} component since the F_y^{stat} component in fact is not a part of the solution, but rather an input of the problem. The agreement between the experiment and the numerical solution is less clean in this case, due to the complex flow evolution in the tank which results in a large number of local minor force peaks. Furthermore, as highlighted in [15] before the first liquid impact the measure of the hydrodynamic component of the vertical force, F_y^{dyn}, is affected by an incorrect overestimation related to the accelerometer measurements and caused by the release mechanism. For this reason this part of the experimental hydrodynamic force is not taken into account when evaluating the external work $\mathcal{W}_{ext}^{dyn}$.

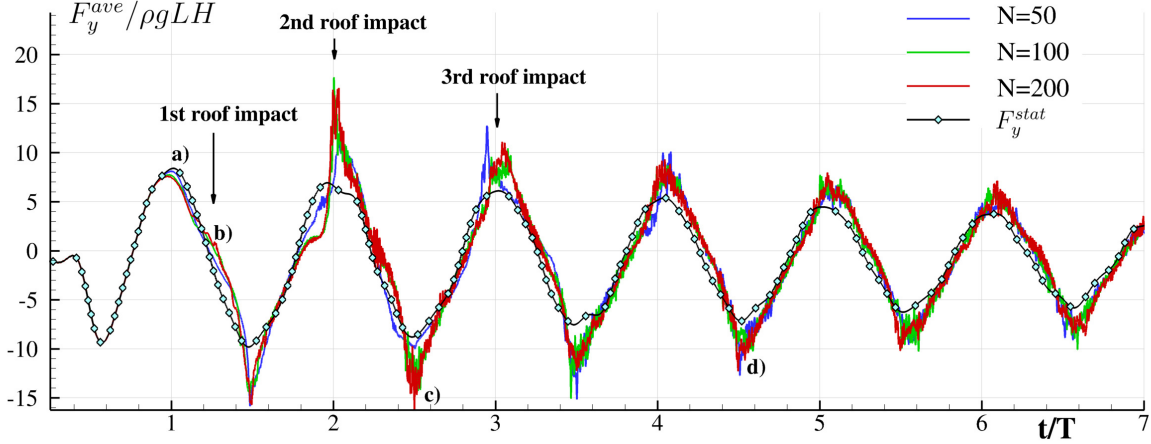In top plot of figure 14 the numerical force F_y^{dyn} is plotted together with the tank velocity.

18

FIG. 12: Ensemble average of the total vertical force for resolutions $N = 50$, $N = 100$, $N = 200$ for Re=233,000. The F_y^{stat} force component is also reported.

In the same plot the first three roof impacts are indicated. The force peak occurring at the first roof impact has the opposite sign to that of the tank velocity. Therefore, a large amount of work done by the solid walls on the fluid is expected during this stage. Conversely, for the second and third peaks a phase shift has occurred and both the force and the velocity have the same sign. The same happens for the subsequent force peaks as well. The corresponding power, $\mathcal{P}_{ext}^{dyn}$, computed as (see Part I):

$$\mathcal{P}_{ext}^{dyn} = v_{tank}\, \boldsymbol{j}\, \cdot \boldsymbol{F}_y^{dyn} \tag{3}$$

is plotted in bottom plot of figure 14. It turns out that, apart from the first roof impacts where a large negative peak is observed (the tank is doing work on the fluid), the roof impacts correspond to positive peaks of $\mathcal{P}_{ext}^{dyn}$ which, conversely, means that the fluid is doing work on the tank. This may appear in contradiction with what shown in Part I: the most intense stages of the flow where energy is dissipated are roof and floor impacts. In fact, to get the full picture of the energy balance, the complete equation has to be considered:

$$- \mathcal{P}_{ext}^{dyn} + \dot{\mathcal{E}}_M^{dyn} + \dot{\mathcal{E}}_C = \mathcal{P}_{diss} \leq 0\,. \tag{4}$$

In figure 15 the terms $-\mathcal{P}_{ext}^{dyn}, -\dot{\mathcal{E}}_M^{dyn}$ and $\mathcal{P}_V$ are plotted (the term $\dot{\mathcal{E}}_C$ being negligible, and thus not relevant to the present discussion). It can be seen that the power related to the energy dissipation $\mathcal{P}_V$ is always negative, as expected. To this end, the term $-\dot{\mathcal{E}}_M^{dyn}$ related to the time derivative of the mechanical energy plays an important role. Indeed, especially
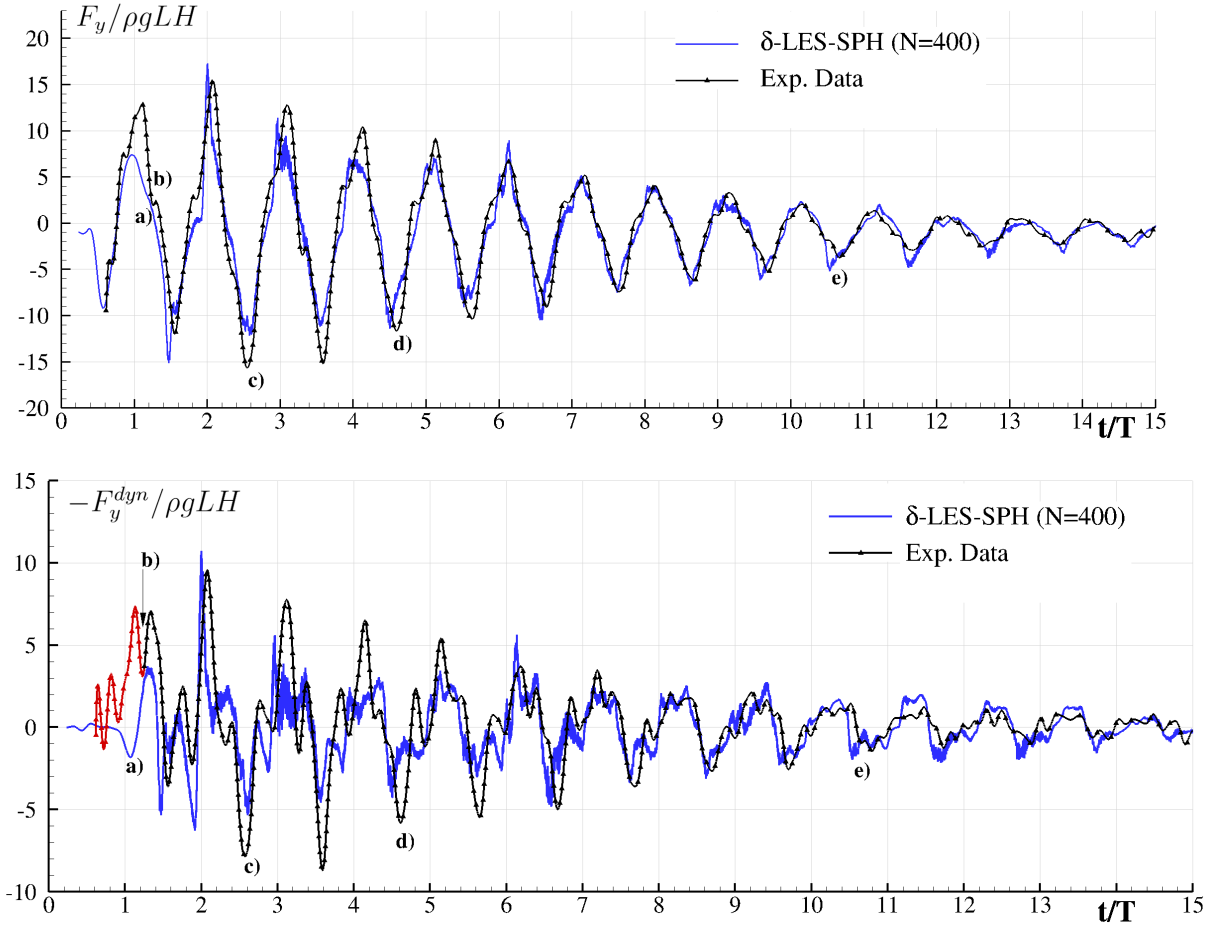
FIG. 13: Force comparison between the experimental data and the SPH simulation at N=400 and Re=233,000: total force (top) and F_y^{dyn} component (bottom). On the bottom plot the initial part of the experimental F_y^{dyn} is colored in red where incorrect overestimation of the force is linked to the release mechanism.

during impacts, this term overshoots the $-\mathcal{P}_{ext}^{dyn}$ term thus always resulting in negative values of the viscous dissipation $\mathcal{P}_{diss}$. Therefore, even if in some impact events a relevant amount of work is done by fluid on the tank, large variations of $\mathcal{E}_M^{dyn}$ guarantee that the energy of the system is always dissipated in those stages as well.

In figure 16 the time histories of the system energy components $\mathcal{E}_M^{dyn}$, $-\mathcal{W}_{ext}^{dyn}$ and $\mathcal{E}_{diss}$ are reported for N=400. These quantities have been obtained by integrating in time the power time histories of figure 15. Remarkably, the mechanical energy $\mathcal{E}_M^{dyn}$ remains limited in time, even though its time derivative can be locally quite high as seen in figure 15. Consequently, the terms $-\mathcal{W}_{ext}^{dyn}$ and $\mathcal{E}_{diss}$ are quite close each other until the end of the simulation when $\mathcal{E}_M^{dyn}$
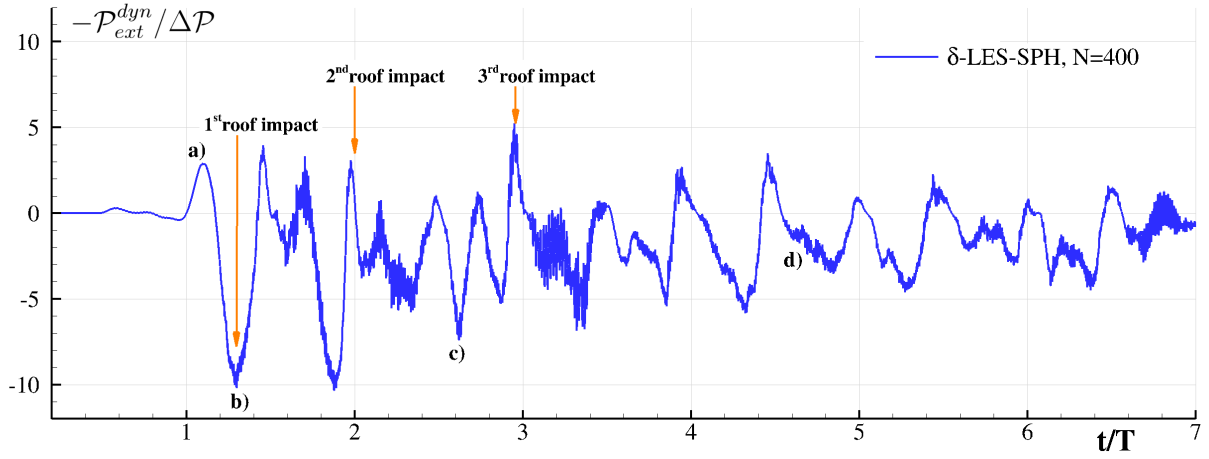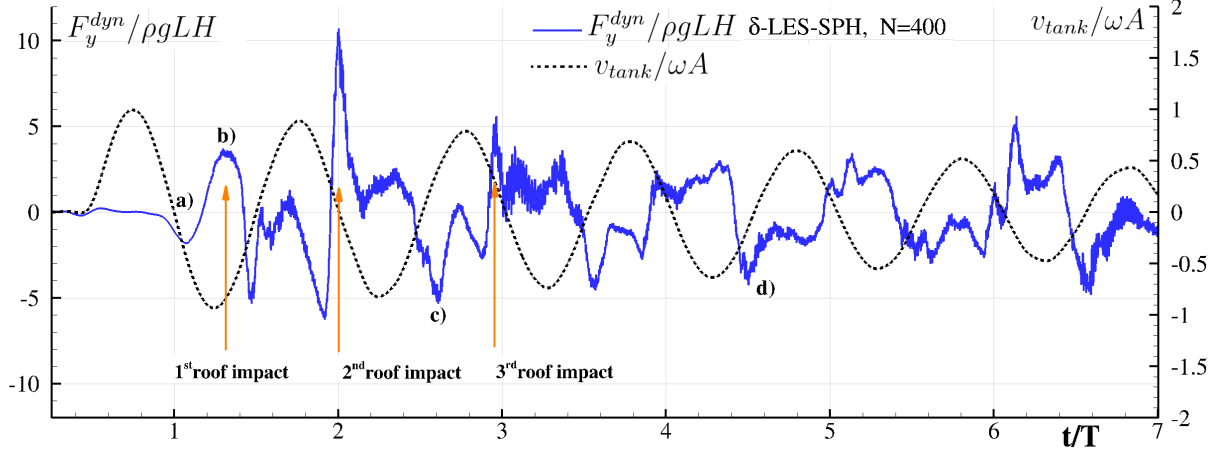
FIG. 14: SPH simulation at N=400 and Re=233,000. Top plot: total force against the tank velocity; bottom plot: time history of the power $-\mathcal{P}_{ext}^{dyn}$ (see definition in the text).
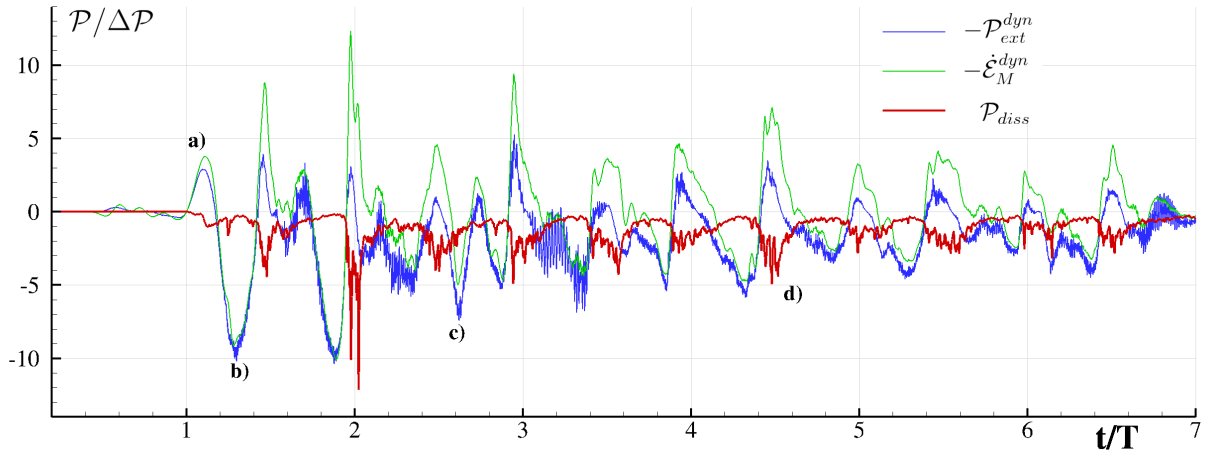

FIG. 15: SPH simulation at N=400 and Re=233,000. Time history of the powers $-\mathcal{P}_{ext}^{dyn}$, $-\dot{\mathcal{E}}_M^{dyn}$ and $\mathcal{P}_V$ (see definitions in the text)
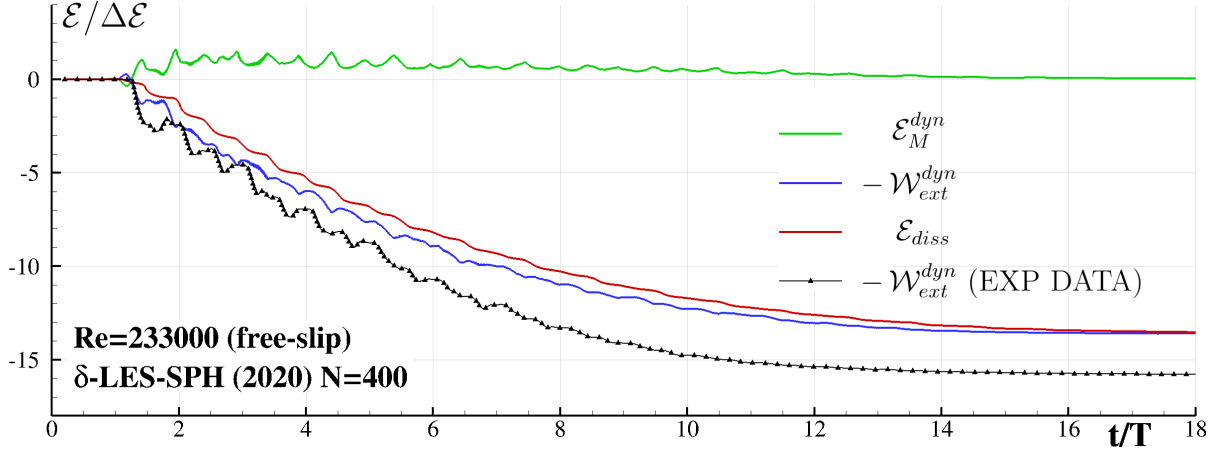
FIG. 16: SPH simulation at N=400 and Re=233,000. Time history of the mechanical energy $\mathcal{E}_M^{dyn}$, the dissipated energy $\mathcal{E}_{diss}$, the external work $\mathcal{W}_{ext}^{dyn}$. The solid line with Δ symbols represents $\mathcal{W}_{ext}^{dyn}$ as computed through the experimental data.

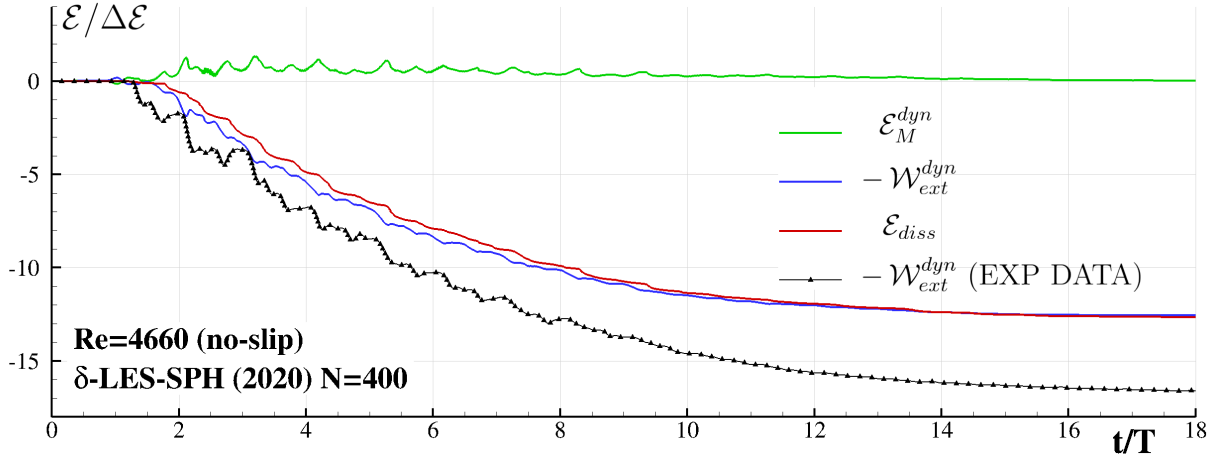FIG. 17: SPH simulation at N=400 and Re=4,660. Time history of the mechanical energy $\mathcal{E}_M^{dyn}$, the dissipated energy $\mathcal{E}_{diss}$, the external work $\mathcal{W}_{ext}^{dyn}$. The solid line with Δ symbols represents $\mathcal{W}_{ext}^{dyn}$ as computed through the experimental data.

becomes null and they coincide. This allows comparison of the dissipated energy evaluated in the numerical simulation with the experimental measurement. Indeed, even if in the experiment it is not possible to measure the quantity $\mathcal{E}_M^{dyn}$, it is possible to estimate $\mathcal{W}_{ext}^{dyn}$ and compare its final value to the numerical counterpart. In figure 16 the experimental $\mathcal{W}_{ext}^{dyn}$ has been depicted. Apart from an initial discrepancy between $t/T = 1$ and $t/T = 2$, due to the observed differences in the force acting at the initial stage of the experiment, the

numerical and experimental curves slightly diverge. The final difference is about 14% of the total dissipated energy.

In figure 17 the same comparison of figure 16 is replicated for the oil simulation at Re=4,660. In this case the experimental and numerical curves related to $\mathcal{W}_{ext}^{dyn}$ are very close each other, up to about $t/T = 5$. Then they start to diverge, and at the end of the simulation the relative error is about 24%. For this case the 3D effects are likely to be more important than for the water test case: wall boundary layers develop also on the front and the rear walls which are not modelled in the present 2D simulation. This aspect will be further investigated in future work where 3D simulations will be performed.

Throughout this session the tank motion has been imposed, and it is important to underline that the experimental measure of $\mathcal{W}_{ext}^{dyn}$ presents various difficulties since even smaller errors on the force and the tank velocity measurements may induce large errors in the evaluation of the external work. To avoid the above drawbacks for the validation of the SPH outputs against the experimental data, in the next section the full FSI problem is studied. Therefore, the tank motion becomes an unknown variable of the problem. Thus, the behaviour of the repeatability of simulations is analysed to assess possible differences with respect to the cases with imposed motion.

B.   Test N.2: Sloshing in coupled motion: comparison with the experimental results

Finally, in this section a set of simulations are carried out this time considering the influence of the liquid on the overall motion of the structure, hence analyzing the coupled system for which the tank motion becomes an unknown. Results will again be compared with experiments to report influence of the coupling on the previous results. The considered system is a 1-DoF system, in the same fashion as is done in the experiments, having the form:

$$F_{\text{slosh}} - B_{0d} \cdot \text{sign}\left(\frac{dy}{dt}\right) - B_{1d} \cdot \frac{dy}{dt} - K \cdot y = m_s \frac{d^2y}{dt^2} \tag{5}$$

where forces coming from different sources that act on the tank are: F_{slosh} is the contribution from the internal fluid action, $K \cdot y$ corresponds to the restoring force that comes from
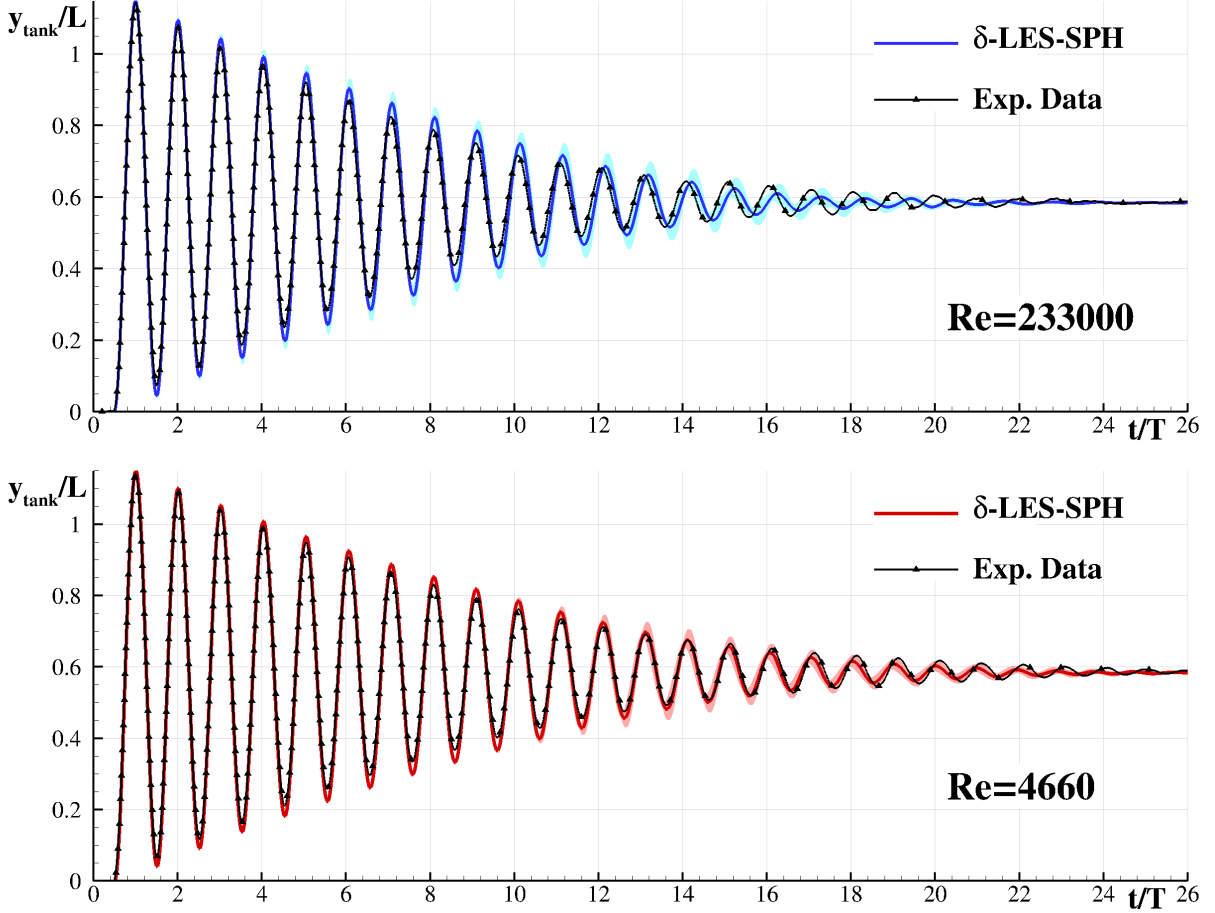
FIG. 18: Evolution of the vertical position of the tank over time obtained from the
FSI-SPH simulation at N=200. Top figure corresponds to Re=233,000 for water and
bottom figure to Re=4,660 for oil. The experimental signal obtained from the
accelerometer is plotted for comparison. Variability of the numerical outcome, represented
in terms of standard deviation, is plotted in lighter color(light blue on the top plot and
pink on the bottom one).

the springs in this particular configuration (see figure 1) and $B_{0d} \cdot \text{sign}\left(\dfrac{dy}{dt}\right) - B_{1d} \cdot \dfrac{dy}{dt}$ is
composed by two terms modelling a Coulomb friction and a viscous friction term respectively.
Both B_{0d} and B_{1d} are coefficients that can be determined experimentally with a dry test,
and do not vary independently with the fluid that is being tested. Hence, determining these
coefficients allows numerical testing of a wide range of fluids and configurations. For this
particular set-up, values for each of these coefficients are $m_s = 2.403$ kg, $K = 4321.62$ N/m,
$B_{0d} = 0.38$ N and $B_{1d} = 1.73$ kg/s.

Figure 18 presents the evolution of the tank vertical position for both cases tested in this work. The top figure shows the water test (Re = 233,000) whilst bottom figure illustrates the oil test (Re = 4,660). In both figures, the tank position obtained from the coupled simulations, in which the forces are computed by SPH, is compared to the ones measured in the experiments. As it can be seen, the agreement between experimental and numerical curves is very good. The numerical curves depicted (blue on the top and red on the bottom) correspond to the ensemble average computed from a set of 10 repetitions in the same fashion as is done in section IV A of the present paper, and in Part I, where variations on the order of 1% are applied to the initial particle positions. Accordingly, variability between the simulations is represented in terms of standard deviation, which is shown in this figure in a lighter color (light blue on the top plot and pink on the bottom one). It is worth noting that the standard deviation increases towards the end of the simulation; this is a consequence of a slight phase shift occurring between the different realizations rather than an actual variation of the motion amplitude. However, from the results in figure 18 it can be observed that the repeatability is high in terms of tank motion when the full coupled system is taken into account. Moreover, results obtained are consistent with previous ones, confirming that variability reduces for the oil case in comparison to the higher Re water case.

The resolution adopted for both test case series is $N = 200$. As discussed in the previous section, this is considered sufficient to obtain results close to convergence. The good agreement shown here between the experimental data and the numerical outcome confirms this estimation. Moreover, two other aspects already discussed in the previous section are confirmed here: i) the 2D SPH simulation predicts a lower dissipation with respect to the experimental case; ii) in the water test case the energy is dissipated more rapidly with respect to the oil case, confirming that in latter case the energy dissipation mechanism is less effective.

V. CONCLUSIONS

The SPH formulation developed in the first part of this paper series for this particular study of violent confined flows has been extended in this second part to forced decay heave motions, confirming that the formulation presented provides a good estimation of the energy

dissipation and of the impact forces for the two different fluids that have been tested in this work. An important difference that can be appreciated with these kinds of time decay laws of motion is that the shaken and sloshing regimes are clearly identified in terms of free surface fragmentation and vorticity fields.

Despite the simplified physical model of the problem that is utilized, including a 2D computational domain, single-phase fluid, lack of surface tension forces or the weakly-compressible fluid assumption, the formulation is able to obtain accurate results, not only with prescribed movement coming from the records registered from the experiments, but also if the tank is coupled to a mass-spring-damper model.

Two different regimes corresponding to two different fluids (water and oil) have been tested. For the water case, Re $\approx O(10^5)$, the maximum numerical resolution adoptes, $N = 400$, exhibits turbulent/ fluid viscosity ratios μ_{turb}/μ of order $\mathcal{O}(1)$ indicating that the inertial turbulent scale is sufficiently resolved while the viscous scale is approximated by the sub-scale model. Conversely, for the oil case, Re $\approx O(10^3)$, the ratio decreases to $\mu_{turb}/\mu = 0.1$, which is close to a DNS description. This is also confirmed because the dependency on the spatial resolution is less significant.

The energy dissipation corresponding to both fluids behaves as expected, and for the largest Reynolds number more than 67% of the total dissipation corresponds to modeled turbulent dissipation and less than 9% is resolved viscous dissipation, while in the oil case these trends invert and 74% corresponds to resolved viscous dissipation and less than 13% to modeled turbulent dissipation. Also, the total dissipated energy measured is larger in the water case than in the oil case, due mainly to the greater amount of energy dissipated during impacts and wave breaking effects that are present in the water test. This result confirms predictions that have been already presented in previous experimental campaigns.

When numerical predictions are compared to experiments, good agreement is obtained in terms of global forces. However, discrepancies are found if the hydrodynamic component of this force, represented by F_{dyn}, is extracted and compared to the experimental version. Complex flow evolution within the tank results in a large number of minor peaks that make the comparison less clean than for the global component.

Also, an interesting conclusion can be drafted from the role of the derivative of the mechanical energy, which keeps a balance with the amount of work done by the fluid on the tank, in order to guarantee the negative sign of the energy dissipation during the complete

simulation.

The time histories of the work done by the system are compared to the experimental estimations, showing a larger discrepancy for the oil case than for the water case, probably due to 3D viscous effects on the walls that are not modelled in this set of 2D cases.

Finally, a fully coupled FSI-SPH simulation is carried out for the same cases. In this case, the tank motion is in principle unknown and has to be computed from the information coming from a mass-spring-damper system and the forces computed by SPH. Results confirm the trends observed for the imposed motion analysis, showing however that the predicted tank motions are less affected by repeatability issues with respect to the forced motion cases and that tank motions time histories are quite close to the ones obtained experimentally. As a final remark, the adopted spatial resolution, which in Part I was shown not to be fine enough to fully resolve all the viscous scales, is indeed sufficient to allow an accurate prediction of the tank motion decay.

ACKNOWLEDGEMENTS

Appendix A: Role of the boundary layer regions on the energy dissipation process

In this section the relevance of the wall boundary layer (WBL) modelling is investigated. As described in section VII of the first part of the paper (Part I), for the considered sloshing case involving water the adopted particle discretization is not fine enough to resolve the WBL. Indeed, for this case the WBL thickness ends up at least one order of magnitude smaller than the finest particle size adopted. In order to further analyse the relevance of WBL, we performed a comparison of the simulation with no-slip and free-slip boundary conditions, being aware of the fact that, in the former case the boundary layers will be overestimated by at least a factor of 10 (in fact it is even larger due to the smoothing action of the SPH kernel). Notwithstanding, the study will give significant indications about the
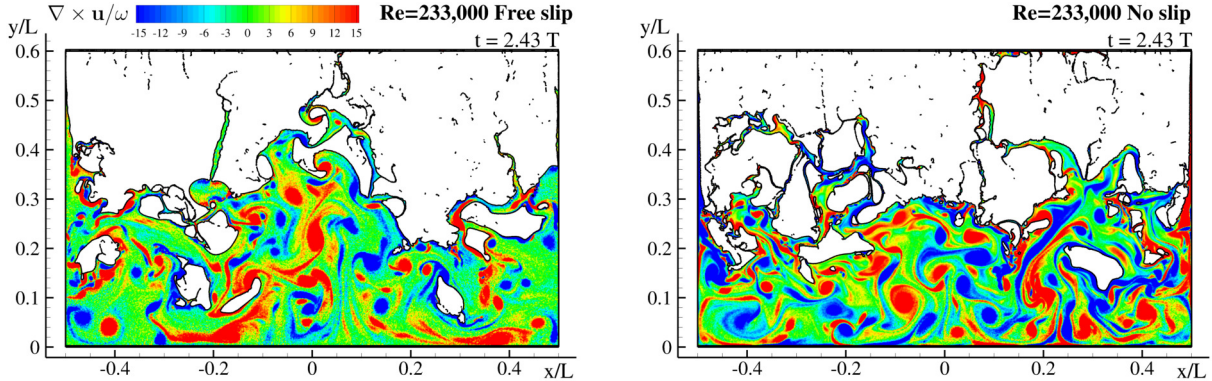
FIG. 19: Vorticity fields of the simulations with free-slip (left plot) and no-slip (right plot) conditions at time $t/T = 2.43$, N=200.

WBL relevance in a conservative sense: if the simulations turn out to be little affected by the presence of an overestimated WBL, one can reasonably expect that the same holds for a WBL ten-times smaller.

In figure 19 the vorticity fields of the simulations with free-slip (left plot) and no-slip (right plot) conditions are reported for time instant $t/T = 2.43$. Regardless, both the vorticity levels and the flow configurations are similar: in the no-slip case the number of vortex structures is larger and the vorticity content is higher. This is mainly due to the vortex sheets generated at the boundaries which detach and roll up, interacting with the pre-existing vortices and eventually moving in the bulk of the flow. Conversely, in the free-slip case the eddies collide against the walls elongating and stretching, but without further production of vortex structures. In the left plot of figure 20 the effect on the energy dissipation of the different boundary conditions is reported. For both free-slip and no-slip cases 10 simulations have been run for the spatial resolution $N = 200$. In the plot the ensemble averages are shown along with the corresponding standard deviation. The two curves are very close: up to about $t/T = 5$, then they slightly diverge, the difference on the final value being about 4% of the total dissipation. This discrepancy is within the standard error obtained for both cases, and is therefore acceptable for the inherent approximations of the simulation. This reasoning applies *a fortiori* if one considers the fact that the boundary layers in the simulation are overestimated by a factor of 10. We note that for this Re number the no-slip case is more dissipative than the free-slip and this fact is likely due to the higher vorticity produced in the field. Furthermore, the no-slip simulation is characterized by a
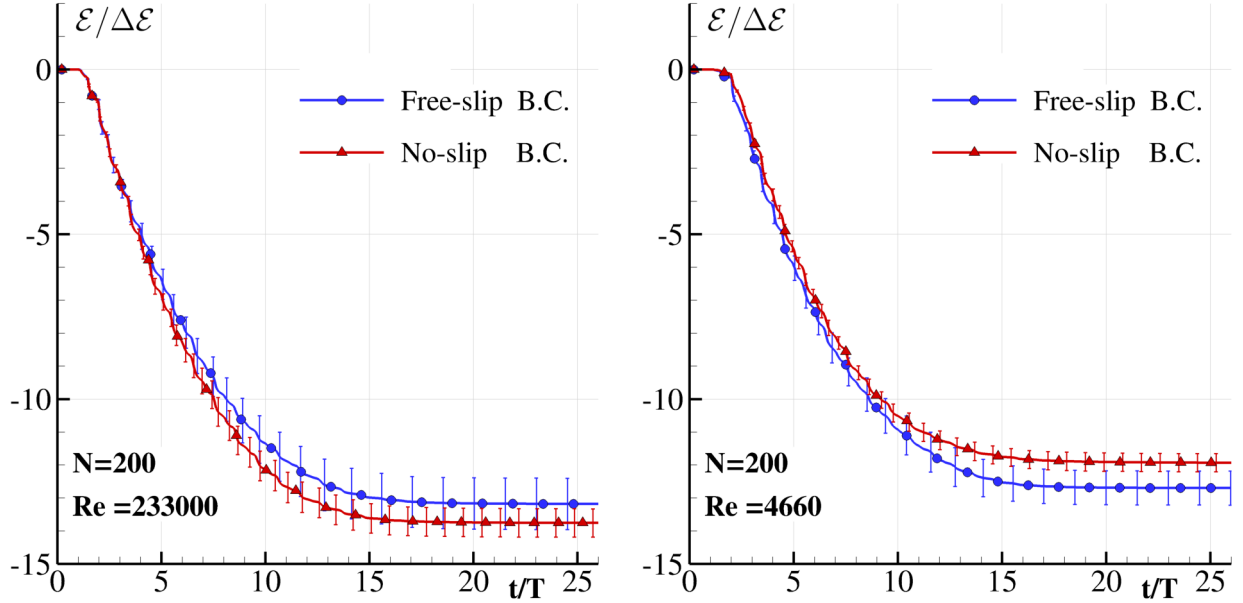
FIG. 20: Time history of the ensemble average of the energy dissipation $\mathcal{E}_{diss}$ for resolutions $N = 200$ using free-slip and no-slip conditions on the solid boundaries. Error bars refer to the computed standard deviation. Left: Re=233,000 for water case. Right: Re=4,660 for oil case.

smaller standard deviation which can be attributed to a stabilising effect of the boundary layers, especially in the initial stages of the flow.

In the right plot of figure 20 the same study has been conducted for the oil case at Re=4,660. In this case the discrepancy is slightly larger (about 6% of the total dissipation), but interestingly, both curves are inverted with respect to the water case, *i.e.*, the free-slip case results the more dissipative condition. This effect is related to the fact that, at this Re, the large boundary layers tend to slow down the flow remarkably, resulting in less energetic impacts, and thus in lower dissipation. This mechanism follows the general behaviour, already observed in [6], for which a higher viscosity leads to lower levels of dissipated energy. We note that also in this case, a smaller standard deviation is observed for the no-slip case with respect to the free-slip one.

[1] H.N. Abramson, W.H. Chu, and L.R. Garza. Liquid sloshing in spherical tanks. *AIAA Journal*, 1(2):384–389, 1963.

[2] M. Antuono, S. Marrone, A. Di Mascio, and A. Colagrossi. Smoothed particle hydrodynamics method from a large eddy simulation perspective. generalization to a quasi-lagrangian model. *Physics of Fluids*, 33(1):015102, 2021.

[3] R.L. Bass, E.B. Bowels, S. Endo, J. Navicakas, J.C. Peck, B.F.M. Pots, R.W. Tudell, N. Yoshimura. Modeling criteria for scaled LNG sloshing experiments. *Transactions of the ASME Journal of Fluids Engineering*, 107, June 1985.

[4] B. Bouscasse, A. Colagrossi, A. Souto-Iglesias, and J. L. Cercos-Pita. Mechanical energy dissipation induced by sloshing and wave breaking in a fully coupled angular motion system. II. Experimental investigation. *Physics of Fluids (1994-present)*, 26(3):–, 2014.

[5] B. Bouscasse, A. Colagrossi, A. Souto-Iglesias, and J.L. Cercos-Pita. Mechanical energy dissipation induced by sloshing and wave breaking in a fully coupled angular motion system. i. theoretical formulation and numerical investigation. *Physics of Fluids*, 26(3):033103, 2014.

[6] B. Bouscasse, A. Colagrossi, A. Souto-Iglesias, and J.L. Cercos-Pita. Mechanical energy dissipation induced by sloshing and wave breaking in a fully coupled angular motion system. ii. experimental investigation. *Physics of Fluids*, 26(3):033104, 2014.

[7] H. Bredmose, M. Brocchini, D.H. Peregrine, and L. Thais. Experimental investigation and numerical modelling of steep forced water waves. *Journal of Fluid Mechanics*, 490:217, 2003.

[8] B. Budiansky. Sloshing of liquids in circular canals and spherical tanks. *Journal of the Aerospace Sciences*, 27(3):161–173, 1960.

[9] J. Calderon-Sanchez, J. Martinez-Carrascal, L. González, and A. Colagrossi. A global analysis of a coupled violent vertical sloshing problem using an SPH methodology. *Engineering Applications of Computational Fluid Mechanics*, 2021.

[10] W.H. Chu. Fuel sloshing in a spherical tank filled to an arbitrary depth. *AIAA Journal*, 2(11):1972–1979, 1964.

[11] L. Constantin, J. de Courcy, B. Titurus, T.C.S. Rendall, and J.E. Cooper. Analysis of damping from vertical sloshing in a SDOF system. *Mechanical Systems and Signal Processing*, 152:107452, 2021.

[12] J.B. Frandsen. Numerical predictions of tuned liquid tank structural systems. *Journal of Fluids and Structures*, 20(3):309–329, 2005.

[13] F. Gambioli, A. Chamos, S. Jones, P. Guthrie, J. Webb, J. Levenhagen, P. Behruzi, F. Mastroddi, A. Malan, S. Longshaw, et al. Sloshing wing dynamics–project overview.

Proceedings of 8th Transport Research Arena TRA 2020, April 27-30, 2020, Helsinki, Finland, 2020.

[14] F. Gambioli and A. Malan. Fuel loads in large civil airplanes. In *International Forum on Aeroelasticity and Structural Dynamics IFASD 2017*, 2017.

[15] J. Martinez-Carrascal and L.M. Gonzalez-Gutierrez. Experimental study of the liquid damping effects on a sdof vertical sloshing tank. *Journal of fluids and structures*, 100, 2021.

[16] S.B. Pope. Ten questions concerning the large-eddy simulation of turbulent flows. *New journal of Physics*, 6(1):35, 2004.

[17] M.J. Tait. Modelling and preliminary design of a structure-TLD system. *Engineering Structures*, 30(10):2644–2655, 2008.

[18] B. Titurus, J.E. Cooper, F. Saltari, F. Mastroddi, and F. Gambioli. Analysis of a sloshing beam experiment. In *International Forum on Aeroelasticity and Structural Dynamics. Savannah, Georgia, USA, paper*, volume 139, 2019.

[19] J.K. Yu, T. Wakahara, and D.A. Reed. A non-linear numerical model of the tuned liquid damper. *Earthquake Engineering and structural dynamics*, 28(6):671–686, 1999.